Journal of Hazardous Materials 476 (2024) 134765

Contents lists available at ScienceDirect

Journal of Hazardous Materials

journal homepage: www.elsevier.com/locate/jhazmat

Heterostructure g-C_3N_4/Bi_2MoO_6 PVDF nanofiber composite membrane for the photodegradation of steroid hormone micropollutants

Zhi-Fu Lin [a,b,c], Han-Ya Lin [a], Ruey-An Doong [b], Andrea I. Schäfer [a,*]

[a] Institute for Advanced Membrane Technology (IAMT), Karlsruhe Institute of Technology (KIT), Hermann-von-Helmholtz-Platz 1, Eggenstein-Leopoldshafen 76344, Germany
[b] Institute of Analytical and Environmental Sciences, National Tsing Hua University, No. 101, Section 2, Kuang-Fu Road, Hsinchu 30044, Taiwan, R.O.C.
[c] International Intercollegiate Ph.D. Program, National Tsing Hua University, No. 101, Section 2, Kuang-Fu Road, Hsinchu 30044, Taiwan, R.O.C.

HIGHLIGHTS

- Steroid hormone degradation in a PVDF-BMCN65/fiber membrane was quantified.
- Heterojunction improves sunlight utilization, and charge recombination rate.
- Immobilization on a nanofiber layer inhibits the self-aggregation of catalysts.
- Material, water chemistry and operational parameters contributed to limiting factors.
- An estradiol removal of up to 96 % was achieved in a continuous-flow reactor.

GRAPHICAL ABSTRACT

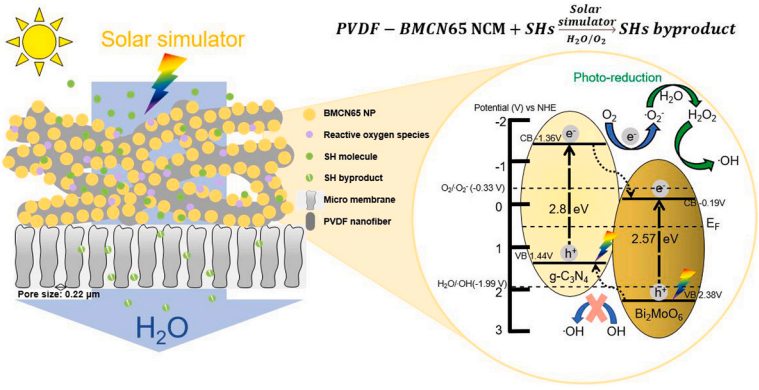

ARTICLE INFO

Keywords:
Heterogeneous photocatalyst
Reactive oxygen species
Flow-through photocatalytic membrane reactor
Micropollutant removal
Physio-chemical water treatment

ABSTRACT

Photocatalytic membrane reactors (PMRs) are a promising technology for micropollutant removal. Sunlight utilization and catalyst surface sites limit photodegradation. A poly(vinylidene fluoride) (PVDF) nanofiber composite membrane (NCM) with immobilized visible-light-responsive g-C_3N_4/Bi_2MoO_6 (BMCN) were developed. Photodegradation of steroid hormones with the PVDF-BMCN NCM was investigated with varying catalyst properties, operating conditions, and relevant solution chemistry under solar irradiation. Increasing CN ratio (0–65 %) enhanced estradiol (E2) degradation from 20 ± 10 to 75 ± 7 % due to improved sunlight utilization and photon lifetime. PVDF nanofibers reduced self-aggregation of catalysts. Hydraulic residence time and light intensity enhanced the photodegradation. With the increasing pH value, the E2 removal decreased from 84 ± 4 to 67 ± 7 % owing to electrical repulsion and thus reduced adsorption between catalysts and E2. A removal of 96 % can be attained at environmentally relevant feed concentration (100 ng.L^{-1}) with a flux of 60 L.m^{-2}.h^{-1}, irradiance of 100 mW.cm^{-2}, and 1 mg.cm^{-2} BMCN65 loading. This confirmed that heterojunction photocatalysts can enhance micropollutants degradation in PMRs.

* Corresponding author.
E-mail address: Andrea.Iris.Schaefer@kit.edu (A.I. Schäfer).

https://doi.org/10.1016/j.jhazmat.2024.134765
Received 20 March 2024; Received in revised form 13 May 2024; Accepted 29 May 2024
Available online 6 June 2024

1. Introduction

1.1. Micropollutants in the environment

Micropollutants, such as endocrine-disrupting chemicals, pharmaceutical and personal care products, and persistent organic pollutants, are a major global challenge and risk to human and environmental health [1–3]. Steroid hormones (SHs) are a prominent group of micropollutants which can affect the endocrine, immune, and nervous systems of humans and animals even at low concentrations, causing endocrine disorders and abnormal regulation of normal hormones [4,5]. Consequently, the World Health Organization (WHO) proposed a guideline concentration (1 $ng.L^{-1}$) for estradiol (E2) in drinking water [6], which posed a treatment challenge. SHs typically entered surface water, groundwater, and drinking water through industrial effluents, agricultural run-off, livestock farms, hospital effluents, and discharge of treated wastewater [6,7]. SHs were not fully removed by conventional wastewater treatment [1–3]. SHs, including E2, estrone (E1), progesterone (P), and testosterone (T), have been widely found at low concentrations (below the physiological levels sub-$ng.L^{-1}$) in the long-term monitoring of wastewater effluent and receiving surface waters [1,2].

1.2. Technologies for micropollutant removal

Various treatment technologies, such as adsorption, membrane filtration, advanced oxidation processes, and biological treatment, have been employed to remove micropollutants [8]. Membrane separation and adsorption technology can remove some micropollutants through size exclusion, electrical repulsion, and adsorption. However, removal is often incomplete [2] and the disposal of concentrates is challenging [3]. Advanced oxidation processes (AOPs), including Fenton oxidation, heterogeneous photocatalysis, and ozonation, can produce the reactive oxygen species (ROS), which can decompose micropollutants into by-products, CO_2 and H_2O through secondary reactions [8]. However, photocatalysts separated from treated wastewater pose a potential risk of secondary contamination in the effluent [9]. Thus, a strategy to overcome the drawbacks of the photocatalyst suspension reactor is combining photocatalysis with a membrane separation process, in form of a photocatalytic membrane reactor [10].

1.3. Photocatalytic membrane reactors

Photocatalytic membrane reactors (PMRs) can be categorized into two main types; i) the suspension of photocatalyst in the reactor solution (slurry-type reactor), and ii) photocatalyst immobilized in/on the membrane (photocatalytic membrane) [9]. Lab-scale photodegradation studies in slurry-type reactors have demonstrated high treatment efficiency of various micropollutants at concentrations ranging from $ng.L^{-1}$ to $mg.L^{-1}$ in the different water sources [11]. This was attributed to the fact that slurry-type reactors can reduce the self-aggregation of catalysts to improve reactive site availability and photocatalytic activity [12,13]. However, suspending photocatalysts may negatively impact water quality, permeate flux, and membrane lifetime due to membrane fouling on the membrane surface [14,15]. In contrast to slurry-type reactors, photocatalytic membranes can effectively minimize the loss of the photocatalyst, ensure continuous operation and reduce membrane fouling, thereby increasing membrane lifetime [16]. Additionally, photocatalysts immobilized in/on the membrane has advantages such as no need to separate and recycle the catalyst, self-cleaning ability, and significantly enhanced mass transfer [17].

1.4. Photocatalyst materials

An ideal photocatalyst can be activated by light with energy ($h\nu$) equal to or larger than its bandgap energy (E_g) to generate an e^-/h^+ pair, the surface/volume charge recombination, the redox reaction, and reactive oxygen species (ROS), as illustrated in Fig. 1 [18]. However, photocatalysts in environmental applications are still constrained by their poor photocatalytic activity [13]. Hence, developing photocatalyst materials with different optical properties, morphologies, and particle sizes is necessary to enhance the photodegradation for micropollutants [18]. Recently, interest in visible-light-driven photocatalysts such as g-C_3N_4 and bismuth-based materials is growing because the narrow band gap can efficiently utilize the solar spectrum [19,20]. Nevertheless, visible-light-driven photocatalysts suffer from a short photon lifetime, which causes poor photodegradation efficiency [21]. Therefore, promising strategies have been developed in the past decade, including decoration by noble metals, doping with additional elements, and forming heterojunctions [21,22]. Among the proposed strategies, engineering heterojunctions and morphology in photocatalysts have proven to be a promising way for environmental applications due to the feasibility and effectiveness for separating e^-/h^+ pairs to enhance the photon lifetime [23].

Heterojunction photocatalysts involved stacking two or more photocatalytic materials with different band gaps over a short distance, which can spontaneously generate electron transfer after light irradiation [24]. The heterojunction occurred through the internal electric field, which caused electrons to spontaneously transfer from the photocatalyst with the higher Fermi level (E_{F1}) to that with lower Fermi level (E_{F2}). Then, the electron transfer reached the equilibrium Fermi level (E_{F3}) to form the heterojunction between photocatalyst and co-catalyst [23]. In general, the electron transfer pathways of different types of heterojunction were described, which can be separated into four types [18]; (a) type-I heterojunction, (b) type-II heterojunction, (c) Schottky junction, and (d) Z-scheme heterojunction. For instance, the combination of g-C_3N_4 and Bi_2MoO_6 can form type II or Z-scheme heterojunction, which significantly enhanced the photocatalytic activity, increases solar energy utilization, and accelerates electron transfer [25,26]. Although Bi_2MoO_6/g-C_3N_4 nanocomposites exhibited the excellent photodegradation performance, the leakage of photocatalysts cause the possible secondary pollution [27]. Therefore, it is essential to develop a photocatalytic composite membrane to prevent leakage of nanoparticles [10], while using g-C_3N_4/Bi_2MoO_6 to attain higher SHs removal in the PMRs.

1.5. Immobilization of photocatalyst onto/into membrane substrate

Photocatalyst immobilization methods can influence light penetration, surface-to-volume ratio, and ROS generation [28]. Typically, these methods can be categorized into two types; (i) entrapment of photocatalyst into the membrane matrix and (ii) disposition of photocatalyst onto the membrane surface [9]. For entrapment, composite membranes were easily fabricated by phase inversion and blending, thus preventing membrane fouling via photodegradation and improving the membrane hydrophilicity [29]. Nonetheless, catalyst loading and particle sizes in the matrix altered membrane morphology and pore size [27], while catalyst surface accessibility may be constrained. In contrast, catalyst disposition onto the membrane surface through the methods such as, chemical grafting, vacuum infiltration, and ALD method, can provide controllable catalyst thickness, anti-fouling performance, and superior chemical stability [30]. Additionally, this method offered advantages such as high catalyst loading, freedom design of morphology, and no impact on the pristine membrane morphology [31,32]. Nonetheless, high catalyst loading faced challenges such as high mass transfer resistance, catalyst self-aggregation, reduced membrane permeability, and limited light absorption [33,34]. Upon comparing photocatalyst entrapment and disposition methods, Bedford *et al.* [35] reported that TiO_2 deposited onto nanofiber had better photodegradation of organic dye under UV irradiation. This was attributed to the high dispersion and loading of TiO_2, which provide excellent photocatalytic activity. Moreover, photocatalysts lost the photocatalytic activity because the polymer matrix reduced the reactive sites of catalysts [36]. While the

immobilized method has been well-established, the nanoparticle size needs to be smaller than the pore size of the supporting membrane. Effective immobilization requires a good interaction between catalyst and support, which mean that it is hard to immobilize a catalyst in the pores of an inert membrane [16]. Therefore, it is essential to develop a membrane substrate with a large specific surface area, high porosity, good affinity for the catalyst and high external mass transfer [37].

1.6. Polymer supporting material and morphology

Polymeric membranes are more widely used as membrane substrates than metal- and ceramic-based membranes because they are flexible, formable, and low-cost [38]. Multiple polymers such as poly(tetrafluoroethylene) (PTFE), poly(acrylonitrile) (PAN), and poly(vinylidene fluoride) (PVDF) have been applied as support materials [39]. In particular, PVDF membrane is a promising candidate for catalytic degradation due to its outstanding chemical resistance to ROS [40]. When the membrane was immobilized with large photocatalysts, the composite membrane will decrease membrane permeability [41]. Consequently, electrospun fibers are ideal support materials for large catalysts due to their open 3D structure, large surface-to-volume ratio, and high porosity [42]. Furthermore, catalysts immobilized onto the fiber surface can enhance the contact between catalysts and micropollutants and reduce the self-aggregation photocatalyst, which was attributed to the well-dispersion onto the fiber surface [43,44]. For example, Liu *et al.* [45] reported that Ag/TiO_2 nanofiber supported by glass filter (pore size: 0.45 μm) performs higher photodegradation performance than P-25 deposited glass filter and TiO_2 nanofiber glass filter under the solar simulator in a dynamic system. Therefore, photocatalysts immobilized onto polymer nanofiber supported by PVDF membrane can effectively improve photocatalytic activity and self-aggregation.

The research aimed to remove steroid hormone micropollutants using photocatalytic membrane under light provided by a solar simulator. $g\text{-}C_3N_4/Bi_2MoO_6$ nanocomposites were immobilized onto PVDF nanofiber composite membrane (NCM) via vacuum filtration method, which can effectively reduce the self-aggregation and leakage of catalyst, while drastically enhancing mass transfer [46]. The performance evaluation using solar simulator and environmentally relevant concentration (100 $ng.L^{-1}$) can establish material and process limitations. How SHs photodegradation efficiency was controlled by i) photocatalytic nanomaterials (catalysts ratio and loading), ii) operating conditions (water flux and light intensity), and iii) solution chemistry (feed concentration, pH, and SHs types) was the primary research interest. The SHs removal in the flow-through PMR operated in a single-pass configuration was investigated as illustrated in Fig. 2.

2. Materials and methods

2.1. Chemicals

Radiolabeled steroid hormones, [2,4,6,7-^{3}H(N)]-Estradiol (3.26 TBq $mmol^{-1}$), [2,4,6,7-^{3}H(N)]-estrone (3.48 TBq $mmol^{-1}$), [1,2,6,7-^{3}H(N)]-testosterone (2.94 TBq $mmol^{-1}$) and [1,2,6,7-^{3}H(N)]-progesterone (3.63 TBq $mmol^{-1}$) were supplied as ethanol solution by Perkin Elmer LAS GmbH, Germany and stored at − 20 °C. Before filtration experiments, the native bottle was diluted with ultrapure water (MilliQ A+ system, Millipore Darmstadt, Germany) stock solution (10 $\mu g.L^{-1}$). Feed solution of a radiolabeled hormone with a concentration of 100 $ng.L^{-1}$ was diluted from the hormone stock solution. For feed concentrations higher than 100 $ng.L^{-1}$, a non-labeled hormone solution was added to increase to obtain the desired feed concentration. Due to the low solubility of SHs in water, a non-labeled hormone solution is prepared in methanol at multiple concentrations (1, 10, 100, 1000, and 10,000 $\mu g.L^{-1}$). Hence, extra methanol (79.2 $mg.L^{-1}$) was added to the feed solution to ensure a constant methanol concentration, while the final ethanol concentration from a native solution was 26.3 $mg.L^{-1}$ in each experiment [47]. The background solution contained 10 mM NaCl (>99.7 %, Merck Millipore, Darmstadt, Germany) and 1 mM $NaHCO_3$ (>99.5 %, Merck Millipore, Darmstadt, Germany) to simulate the natural water. However, the organic solution and inorganic ions can quench the ROS with quenching rate constants (k) for hydroxyl radicals of Cl^- ($k = 4.3\bullet10^9$ $M^{-1}.s^{-1}$), methanol ($k = 9.7\bullet10^8$ $M^{-1}.s^{-1}$), and ethanol ($k = 2.8\bullet10^9$ $M^{-1}.s^{-1}$). Furthermore, the HCO_3^- can quench the hydroxyl radicals ($k = 8.5\bullet10^6$ $M^{-1}.s^{-1}$) and electrons ($k = 6\bullet10^5$ $M^{-1}.s^{-1}$) [48].

For the pH adjustment of feed solutions 1 M HCl (33.7 %, Carl Roth,

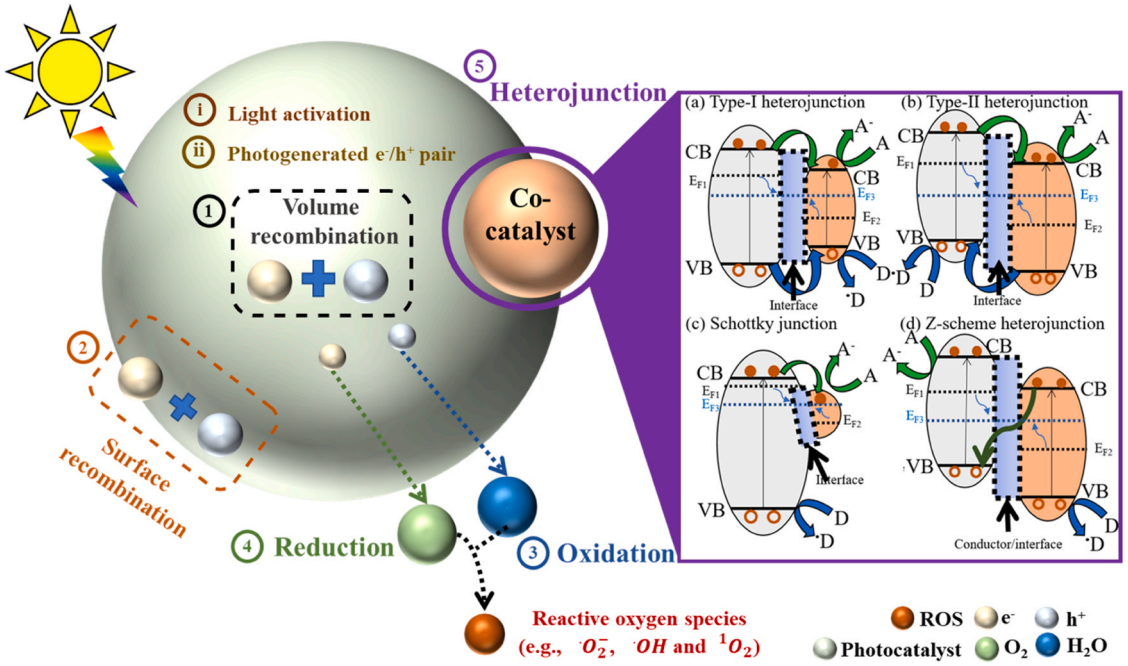

Fig. 1. The mechanism of heterojunction photocatalysts. D electron donor; A electron acceptor; CB conduction band; VB valance band; Fermi energy (E_F) is the difference between the highest and lowest occupied single-particle states in a quantum system of non-interacting fermions at absolute zero temperature [23].

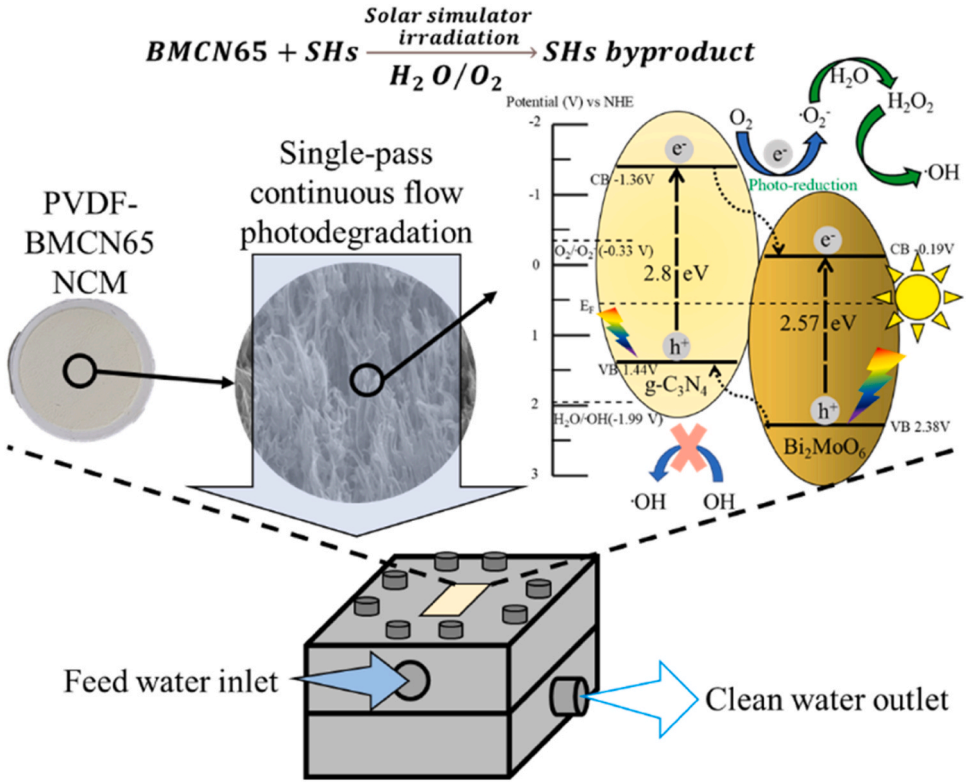

Fig. 2. Schematic of a photocatalytic membrane reactor and PVDF-BMCN65 NCM for single-pass continuous flow micropollutant photodegradation.

Karlsruhe, Germany) and 1 M NaOH (99 %, Merck Millipore, Darmstadt, Germany) prepared in Milli-Q water are used.

2.2. Preparation of photocatalyst, nanofiber, and composite membrane

The g-C_3N_4 (CN) was prepared through thermal pyrolysis and thermal exfoliation. Notably, 10 g urea (J.T.Baker, 99 %, USA) in a boat crucible was heated to 550 ℃ at 10 ℃.min^{-1} in the muffle furnace (DF40, DENG YNG, Taiwan) and kept at 550 ℃ for 2 h to obtain bulk CN. The box furnace was cooled by radiation to room temperature. After room temperature, the bulk CN was heated to 450 ℃ at 10 ℃.min^{-1} for 2 h in the muffle furnace (DF40, DENG YNG, Taiwan) to obtain CN nanosheet [49].

Briefly, 2 mmol $Bi(NO_3)_3$•5 H_2O (Alfa Aesar, 98 %, USA) was mixed with 1 mmol Na_2MoO_4•2 H_2O (Alfa Aesar, 98 %, USA) in a 30 mL solution (diethylene glycol (Alfa Aesar, 99 %, USA): ethanol (Alfa Aesar, 99 %, USA) = 1:1) with vigorous stirring for 1 h. It was then transferred to 50 mL Teflon tubes at 160 ℃ for 4 h. The obtained Bi_2MoO_6 (BMO) precipitate was washed 3 times with Milli-Q (18.2 Ω, Merck, USA) and ethanol (Alfa Aesar, 99 %, USA) to remove the no reactant by the centrifuge. The BMO particle was dried at 60 ℃ for 12 h [49].

A 21 % (w/v) PVDF (1015/1001, Solvay, Belgium) solution was prepared by dissolving in DMF/Acetone (9:1) at 65 ℃ on the magnetic stirrer (300 rpm, SU1300, Sustainable Lab Instruments, Germany) for 24 h. After dissolving, the solution was cooled to room temperature for 1 h. The PVDF nanofiber was electrospun directly onto the PVDF membrane (0.22 μm, hydrophobic, Millipore, USA) by an electrospinning machine, which contained a syringe pump (LA100, Landgraf Labor system HLL GmbH, Germany), a collector with an x-y controller (SMC 200, MOVTEC Wacht GmbH, Germany), and a power supply (HPC-14–20000, FuG Elektronik GmbH, Germany)). The voltage was set to 15 kV, the flow rate was set to 0.5 mL.h^{-1}, and the distance from the collector was set to 20 cm. After the fabrication, the PVDF nanofiber support PVDF membrane (PVDF-fiber) was dried at 60 ℃ for 12 h in the oven.

For the photocatalysts suspended solution, TiO_2 (300 nm, 100 % anatase, CD bioparticle, USA), CN, BMO, and mixed BMO/CN solutions with various weight ratios of CN: BMO (80:20, 75:25, 70:30, 65:35, 60:40, 50:50, 40:60, 30:70, and 20:80 wt%:wt%), were measured by the balance (Adventurer AX622/E, Ohaus, Germany). The suspended solution was prepared by sonicating a mixture of 0.1 g.L^{-1} in Milli-Q water. A circular piece of the fiber/PVDF membrane with 66 mm diameter was placed on a stainless-steel support layer (Millipore, Germany) inside a ceramic funnel. The suspension was loaded onto the membrane via a vacuum filtration apparatus (vacuum pump, FB70155, Fisherbrand, Germany). The loaded volumes of 34.2–239.4 mL of the 0.1 g.L^{-1} suspension were related to a photocatalysts loading of 0.25–1.75 mg.cm^{-2}. Each photocatalytic membrane coupon was cut into 4 pieces of 25 mm (4.9 cm^2) diameter. The composite membranes were generated from CN, BMO, and the mixer of BMO/CN. According to the CN, BMO, and CN ratio of mixer, photocatalytic composite membranes are named as TiO_2, CN, BMO, and BMCNX (X = 80, 75, 70, 65, 60, 50, 40, 30, 20), respectively.

2.3. Characterization of photocatalyst, nanofiber, and composite membrane

The cross-section and morphology of photocatalysts and photocatalytic membranes were determined by a cold field emission scanning electron microscope (SEM, SU-8010 Hitachi, Japan), operated at a voltage of 15 kV in Fig. S5. Before this analysis, the samples were sputter-coated with a 10 nm platinum surface film with a JFC-1600 Auto Fine Coater (JEOL, Japan). Powder X-ray diffraction patterns were measured by an X-ray diffractometer (D8, Bruker, Germany) with Cu Kα radiation (λ = 1.5406 Å) at 40 mA and 40 kV to identify the crystallinity and phase of photocatalysts and photocatalytic membranes in Fig. S2. The photocatalytic membrane was placed into a Fourier-transform infrared spectroscopy (FTIR, Spectrum Two, Waltham, Perkin Elmer) to measure the bond formation and functional groups in Fig. S3. The surface charge of membranes was determined in the electrolyte

containing 0.001 mM KCl with Zetasizer (Nano-ZS ZEN 3600, Malvern, UK), where the membrane was placed into Zetasizer Cuvettes (DTS1070, Malvern, UK, see Fig. S6). The photocatalytic membrane was place into thermogravimetric analyzer (TGA, TG 209 F1 Libra, Netsch, Germany) to measure the weight loss of membrane before/after experiment in Fig. S14.

Optical properties characterization of photocatalytic membranes was determined by the absorption spectrum and the diffuse reflectance spectrum with a UV/visible spectrometer (U-4100, Hitachi, Japan) in Fig. S7. The membrane was placed in the circle holder covered with quartz glass of 18 mm diameter in the solid mode to measure the absorption and reflectance spectrum. A time-resolved-PL spectrometer (tr-PL, iHR550, Horiba Jobin Yvon, Japan), based on a time-correlated single-photon counting method, equipped with a laser (405 nm) as an excitation source, was employed to characterize excited free-carrier dynamics about the pumping intensity. The photocatalytic membrane was placed into the glass tube, where a Xe lamp (350 W) was the light source to activate the photocatalytic membrane. The CCD detector (400–1000 nm) and a cooled InGaAs detector (800–1600 nm) determined the photon lifetime in Fig. S8. Ultraviolet photoelectron (UPS) and X-ray photoelectron spectroscopy (XPS) were investigated on ESCA PHI 1600, Thermo Fisher Scientific, USA with ultra-violet He source was used to determine the position of valence bands and surface chemical compositional states of the photocatalytic membrane in Fig. S10A and Fig. S4. The photocatalytic membrane was placed onto the copper film and is dried at 60 ℃ in the oven for 12 h. The membrane was transferred into UPS, which was carried out with a helium discharge lamp ($h\nu$=21.22 eV) in normal emission) at a high vacuum value. The VB position (VB-XPS, Fig. S10B) was determined by linear extrapolation of the valance band onset subtracted from the background. UV/Visible transmittance spectra (Lambda-950 spectrophotometer, Perkin Elmer, Waltham, USA) were measured by placing membranes on the transmittance sample holder to determine the light penetration of BMCN membranes from 200 to 800 nm in Fig. S12.

All the electrochemical experiments (Fig. S9) were investigated at room temperature by Autolab (Metrohm, USA). After mixing active material and Nafion in an isopropanol solution, this mixture was well-mixed into a homogeneous slurry by ultrasonication. For the working electrode coating, the slurry was pasted onto 1 × 1 cm^2 FTO glass via the spin-coating method, and the working electrode was dried overnight at 60 °C under the vacuum. The loading mass of the electrode was controlled at 1 $mg.cm^{-2}$. Moreover, the Ag/AgCl and Pt electrodes served as the reference and counter electrodes.

10 mM 5,5-dimethyl-1-pyrroline N-oxide (DMPO) was prepared in DI water or dimethyl sulfoxide (DMSO) as the scavengers to trap free radicals, including $^{\bullet}OH$ and $^{\bullet}O_2^-$, respectively. The photocatalytic membrane (1 ×2 cm^2) was placed into the DMPO solution, and a Xe lamp (350 W, Jiehan SS-1050, Taiwan) was then used as the light source to activate the photocatalytic membrane. The solution of 1 mL was quickly extracted and transferred into the glass tube. EPR spectra (Bruker E-580 spectrometer, Germany) were taken to determine the free radicals (Fig. S11). Mercury intrusion porosimetry (MIP, Thermo Scientific, USA) analysis provided the pore size, pore volume, and porosity (ε_p) of nanocomposite membrane. The mercury filled the void space on the surface of the sample. MIP can characterize pore diameters in the size range of 4 nm to 200 μm. Large pores typically require less pressure (and time) to fill with mercury than smaller ones. Hence, the pore size distribution and porosity (ε_p) were determined (Table S8).

2.4. Photocatalytic membrane filtration system and filtration protocols

The experiments to evaluate the photodegradation of SHs were conducted in a custom-built flow-through filtration system (Fig. 3 and Fig. S1) and the filtration protocol was shown in Table S2 [47]. The feed solution was placed into a 1 L double-jacketed beaker with temperature controlled by a chiller (mini-chiller 300 OLE, Huber, Berching, Germany). A stainless-steel membrane cell with a quartz window (thickness 2 cm, active area 2 cm^2, Zell Quarzglas, Geesthacht, Germany) was designed for illumination of the photocatalytic membrane in-situ. A HPLC pump (BlueShadow Pump 80 P, pump head 500 mL, Knauer) provided flow and pressure, while a solar simulator (Wavelength from 350 to 1150 nm, SolSim, SINUS-70, Wavelabs, Germany) served as the light source for the illumination of the photocatalytic membrane. The spectrum of the solar simulator was described in Fig. S15. The 16-port switching valve (Azura, V 2.1 S, Knauer, Berlin, Germany) collected the permeate sample at different times. A pressure sensor (Type A-10,

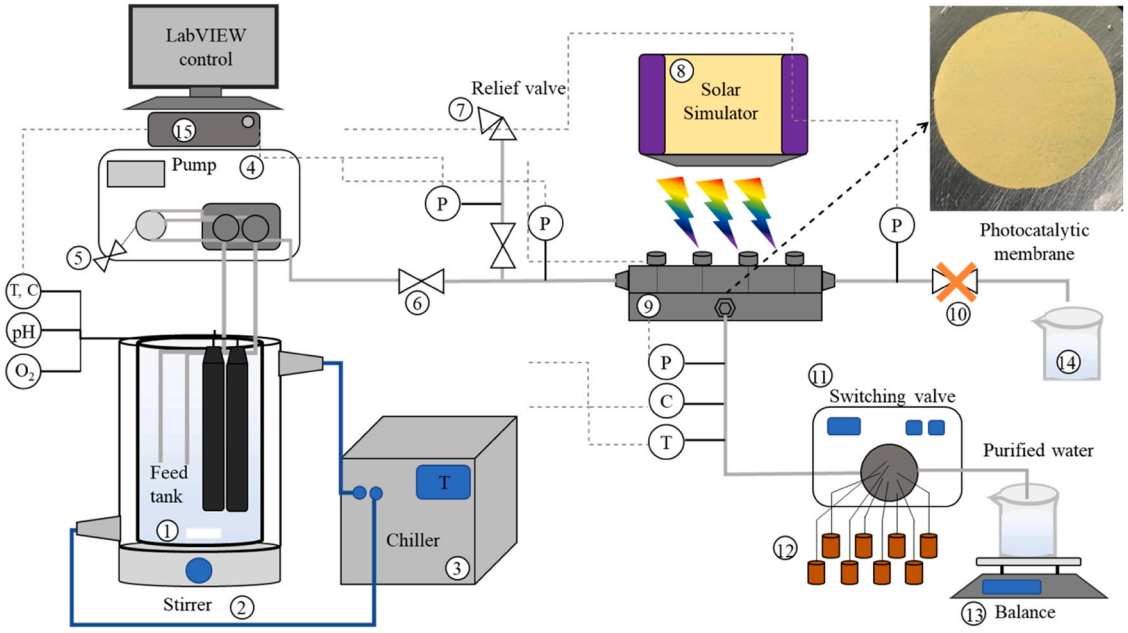

Fig. 3. Scheme of photocatalytic membrane system, 1) feed tank (double jacketed beaker), 2) magnetic stirrer, 3) chiller, 4) HPLC pump, 5) purge valve, 6) pump shut-off valve, 7) low-pressure sensor with shut-off-valve and low-pressure relief valve, 8) Solar simulator 9) photocatalytic membrane cell, 10) retentate needle valve, 11) 16 port switching valve, 12) permeate vials, 13) balance, 14) retentate tank, 15) computer.

WIKA Alexander Wiegand SE & Co. KG, Klingenberg, Germany) was applied to monitor the transmembrane pressure, a conductivity sensor (ET131, eDAQ, Colorado Springs, USA) and thermocouple (NI USB-TC01, NI, Austin, USA) measure conductivity and temperature in the system. The permeate mass was determined by balance, and the permeate flow rate calculated. LabVIEW software (version 2016, NI, Austin, USA) was used for system control and data acquisition (USB-6000, NI, Austin, USA) except pH value and dissolved oxygen concentration, which were recorded manually as described below. The filtration has been adapted from prior work (Table S3) [46]. After membrane compaction, permeability was measured at various flow rates prior to experiments to ensure there are no leakages in the system and the membrane has no defects. The total permeate volume was 700 mL the first 100 mL were filtered in the dark phase to reach SH adsorption equilibrium, followed 600 mL after turning on the solar simulator. The samples were kept in the light-resistant vials at 4 ℃ fridge prior to analysis.

The standard conditions were set as follows; flow rate 2 mL.min^{-1} (flux 600 L.m^{-2}.h^{-1}), E2 concentration 100 ng.L^{-1}, light intensity 8 mW.cm^{-2}, pH 8.2 ± 0.4, 23 ± 0.2 ℃, 1 mM $NaHCO_3$, and 10 mM NaCl. The integrity of the membranes was evaluated by measuring pure water flux before and after filtration.

2.5. Water quality analysis

Ultra-high-pressure liquid chromatography with flow scintillation analysis (UHPLC-FSA, Perkin Elmer, USA) was used for the separation and quantification of the radiolabeled steroid hormones. The SHs were separated by UHPLC using MeOH/water as eluent with 40–80 % gradient of MeOH over 25 mins. This gradient step was followed by 15 min of washing with MeOH/water with 40 % of the MeOH mobile phase. The mobile phase was mixed with scintillation liquid (Ultima-Flo M, Perkin Elmer, USA). The samples (200 μL) are injected into the UHPLC-FSA system to enhance the LOD [47]. Methylene blue concentrations were determined with a UV/Vis spectrophotometer (Lambda 365, Perkin Elmer, USA) equipped with a flow-through cuvette (light path of 10 mm, Hellma Analytics) and a reference cuvette filled with Milli-Q water. The absorbance was measured at the wavelength of 664 nm for methylene blue [50]. pH value and dissolved oxygen concentration data were recorded manually by a pH meter (pH/cond 3320, WTW, Germany) equipped with a glass electrode (SenTix81, WTW, Germany) and a multiparameter meter (Multiline 3510 IDS, WTW, Germany) equipped with an oxygen sensor (FDO-925, WTW, Germany). The equations for calculating membrane performance and apparent photocatalysis kinetics were detailed in Table S1.

3. Results and discussion

The purpose of this work was to investigate if the novel PVDF-BMCN65 nanofiber composite membrane (NCM) can achieve enhanced performance with solar simulator irradiation compared to PVDF-TiO_2 photocatalytic membranes.

3.1. Comparison of E2 removal with the different photocatalytic membranes

In the first instance, it is necessary to know if the heterojunction photocatalysts can improve photodegradation performance compared to TiO_2. For this purpose, a TiO_2 with identical particle size (100 % anatase), and thus surface area, was chosen and loaded into the NCM. E2 removal by the PVDF-TiO_2 and PVDF-BMCN65 NCM was investigated in the flow-through PMR irradiated with both UV (365 nm) light and solar simulator (350 - 1150 nm, Fig. 4).

Prior to exposure to light irradiation, saturation of E2 adsorption was achieved by both PVDF-TiO_2 and PVDF-BMCN65 NCM, which was obvious by permeate (c_p) and feed concentration (c_f) becoming equal.

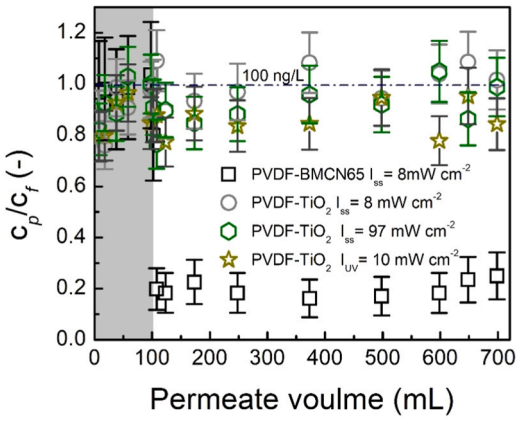

Fig. 4. E2 Normalized concentration ratio (c_p/c_f) of PVDF-BMCN65 NCM and PVDF-TiO_2 (100 % anatase, 300 nm) as a function of permeate volume. (loading 1 mg.cm^{-2}, solar simulator (SS) irradiance 8 or 97 mW.cm^{-2} (350 - 1150 nm), UV (365 nm) irradiance 10 mW.cm^{-2}, flux 600 L.m^{-2}.h^{-1}, flow rate 2 mL.min^{-1}, pH 8.2 ± 0.4, 24 ± 2 °C, E2 concentration 100 ng.L^{-1}, 1 mM $NaHCO_3$, 10 mM NaCl, 27.2 mg.L^{-1} EtOH, 79.2 mg.L^{-1} MeOH.).

When turning on the light source, the normalized concentration ratios over the PVDF-TiO_2 membrane under the solar simulator at 8 or 97 mW.cm^{-2} decreased to a concentration ratio of 1 ± 0.12 and 0.86 ± 0.1 (R= 0 ± 12 and 14 ± 10 %), respectively, indicating very low removal. With the UV lamp at 10 mW.cm^{-2}, removal efficiency was 10 ± 11 %, surprisingly and significantly lower than that of 30 nm TiO_2 particles (R = 79 ± 4 %) [51] under the same photocatalytic filtration conditions. This lower performance was attributed to the larger particle size and the fact that the crystal phase of this TiO_2 was anatase. In previous work [46,51], TiO_2 contained three crystal phases (80 % anatase, 15 % brookite, and 5 % rutile), and Preethi *et al.* [52] indicated that triphasic TiO_2 can form heterojunctions between different crystal phases and enhance the photocatalytic activity.

The PVDF-BMCN65 NCM was investigated with 8 mW.cm^{-2} solar simulator irradiation, resulting in a normalized concentration ratio of 0.25 ± 0.06 (R=75 ± 6 %), this a significantly enhanced degradation. These results indicated that BMCN 65 (visible-light-response heterojunction photocatalyst) has a higher E2 removal efficiency than TiO_2 (UV-light-response photocatalyst), significantly enhancing photocatalytic activity. This observation confirmed prior reports of the methylene blue photodegradation efficiency in a suspension system that a g-C_3N_4/Bi_2MoO_6 nanocomposite being 5 times higher than that of P25 TiO_2 [25].

It is noted that both particle size and heterojunction can contribute to the difference in photocatalytic activity. Therefore, optimizing the CN ratio of g-C_3N_4/Bi_2MoO_6 composites is one important impact factor for enhancing the photodegradation performance.

3.2. Contribution of CN ratio in BMCNX heterojunction photocatalysts

Heterojunction photocatalyst after light irradiation can form an internal electric field between catalyst surfaces, where the electron simultaneously transferred to form a heterojunction. The heterojunction can improve the charge recombination rate, solar light utilization, photocatalytic activity, and photon lifetime [26]. Heterojunction photocatalysts were fabricated in a certain photocatalyst ratio between CN and BMO. To determine the best photocatalyst ratio in removing E2, a series of CN ratios in heterojunction photocatalyst were investigated in Fig. 5. Normalized parameters (c_p/c_f, temperature, conductivity and transmembrane pressure) as function of permeate volume for PVDF-BMCN NCM can be found in Fig. S16, Fig. S17, Fig. S18, and Fig. S19.

The CN ratio of g-C_3N_4/Bi_2MoO_6 composites (0 to 100 %) can be

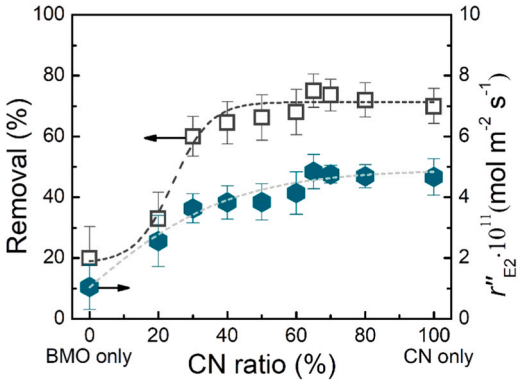

Fig. 5. E2 removal and rate of disappearance as a function of CN ratio. (PVDF-BMCNX NCM, loading 1 mg.cm^{-2}, irradiance 8 mW.cm^{-2} (350 - 1150 nm), flux 600 L.m^{-2}.h^{-1}, flow rate 2 mL.min^{-1}, pH 8.2 ± 0.4, 24 ± 2 °C, E2 concentration 100 ng.L^{-1}, 1 mM $NaHCO_3$, 10 mM NaCl, 27.2 mg.L^{-1} EtOH, 79.2 mg.L^{-1} MeOH).

separated into two regimes in terms of E2 removal and rate of disappearance (r'') (see **Eq.S5**). When PVDF-BMCNX NCM increased from 0 to 50 %, the E2 removal increased consistently from 20 ± 10 to 66 ± 7 %. Once the CN ratio in BMCNX was more than 50 %, E2 removal over PVDF-BMCNX NCM exhibited more than 66 %. This observation was the same in that the high ratio of CN can provide higher photocatalytic activity [53]. Moreover, r'' was around 4 times higher than "BMO only" (r''= (1.04 ± 0.7)·10^{11} mol.m^{-2}.s^{-1}) when the CN ratio was more than 50 % (r''= (3.84 ± 0.6)·10^{11} mol.m^{-2}.s^{-1}), which was attributed to the heterojunction in photocatalysts [54]. To gain deep insight into different CN ratios and optimize the CN ratio, the CN ratio experiment was further examined by methylene blue (c_f=1 mg.L^{-1}) experiments (Fig. S20), in which the PVDF-BMCN65 NCM also exhibited the highest removal efficiency (R= 24 ± 7 %). The above increased removal can be attributed to the combination of g-C_3N_4/Bi_2MoO_6 nanocomposites. The g-C_3N_4/Bi_2MoO_6 nanocomposite exhibited an enhancement of optical properties in that it enhanced light absorbance in the region of 440 (CN) to 483 (BMCN65) nm (Fig. S7A), decreased the band gap significantly from 2.8 (CN) to 2.64 (BMCN65) eV (Fig. S7B), and increased photon lifetime from 2.36 (BMO) to 5.97 (BMCN65) ns (Fig. S8). Furthermore, the photoelectrochemical analysis displayed that BMCN65 has the highest photocurrent density (Fig. S9A) and the lowest R_{ct} value (Fig. S9B) than CN and BMO. Above results can be attributed to the fact that heterojunction in BMCN65 can enhance the photocatalytic activity, light utilization, the charge separation efficiency, and the migration of charge carriers [54].

To further confirm the heterojunction formation in BMCN65, XPS analysis was evaluated the surface chemical composition of photocatalysts. As shown in Fig. S4, all XPS peak positions considerably shifted, which can prove the successful formation of heterojunction in BMCN65 [25]. To propose a possible photocatalytic reaction mechanism, the band structure of photocatalysts was estimated by UPS spectrum (Fig. S10A), VB-XPS spectrum (Fig. S10B), and DRS spectrum (Fig. S7B). As shown in Table S5, the VB positions of CN and BMO were respectively + 1.44 and + 2.38 V. Based on the E_{VB} and E_g values, the CB position for CN and BMO were calculated as − 1.36 and − 0.19 V, respectively. Before contacting BMO and CN, the band structures were independent, which indicated that photocatalysts didn't interact on the photocatalyst surface. After establishing contact between the photocatalysts, the combination can form type-II and Z-scheme heterojunctions. For type-II heterojunctions (Fig. 6a), the photo-induced hole migrated from + 2.38 V (VB of BMO) to + 1.44 V (VB of CN), while the photo-excited electron transferred from − 1.36 V (CB of CN) to − 0.12 V (CB of BMO). Under these circumstances, the photo-excited electrons can react with O_2 to produce $^{\bullet}O_2^-$ ($E_{O2/\bullet O2-}$= −0.33 V vs NHE) and photo-induced holes in the VB of CN (+1.44 V vs NHE) cannot react with water to generate $^{\bullet}$OH ($E_{H2O/\bullet OH}$= +1.99 V vs NHE) [55]. Meanwhile, the remaining electrons in these heterojunctions can react with water to produce a small amount of $^{\bullet}$OH. For Z-scheme heterojunctions (Fig. 6b), both BMO and CN can produce e^-/h^+ pairs in their band structures under solar simulator irradiation. The photo-excited electron in the CB of BMO transferred to the VB of CN, and then reacted with photo-induced hole in the VB of CN. Therefore, holes in the VB of BMO can react with water to produce $^{\bullet}$OH and the remaining electron in the CB of CN can reduce O_2 to produce $^{\bullet}O_2^-$, H_2O_2 and $^{\bullet}$OH [26].

To further confirm which type of heterojunction was formed between CN and BMO, the generation of ROS species was further identified by EPR spectra. The EPR spectra were measured in DMSO and DI solution with 10 mM DMPO to detect the presence of $^{\bullet}O_2^-$ and $^{\bullet}$OH, respectively. As shown in Fig. S11, the unique peaks of DMPO-$^{\bullet}O_2^-$ (signal

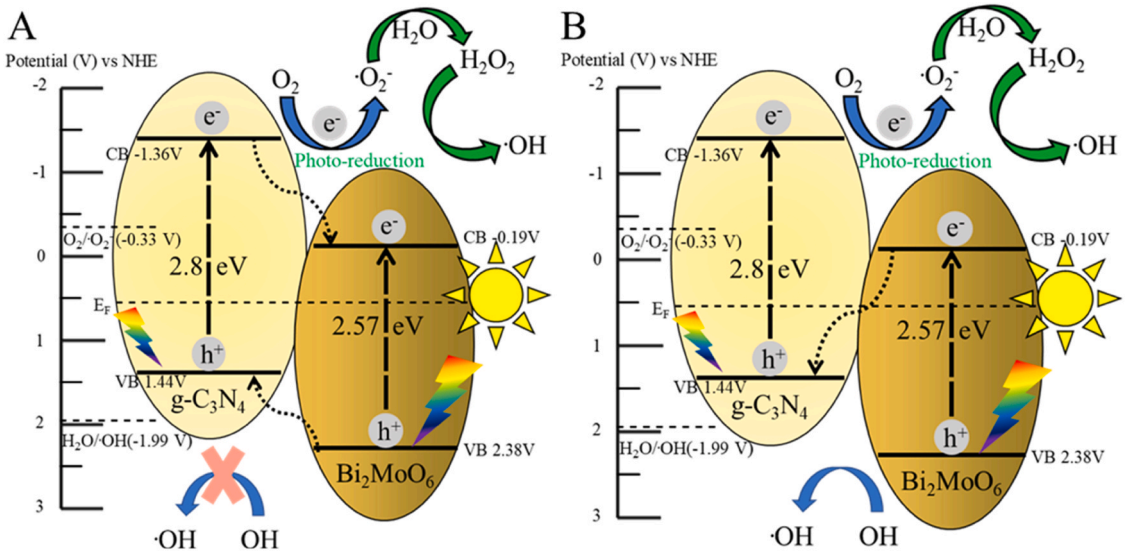

Fig. 6. Possible photocatalytic mechanism scheme of BMCNX heterojunction photocatalyst. A: type-II heterojunction. B: Z-scheme heterojunction. VB: valance band. CB: conduction band.

splitting1:2:2:1) and DMPO-•OH (signal splitting1:1:1:1) were obvious in the spectra after light irradiation [49]. However, the peak of DMPO-•OH was very small, indicating that the quantification of •OH was low. According to the above description of heterojunctions, the heterojunction of BMCN65 can be proved as the type-II heterojunction, which can generate $^{\bullet}O_2^-$ and the low concentration of •OH. Moreover, $^{\bullet}O_2^-$ radicals can be considered as the primary reactive radical during the photodegradation, which the organic solvents and inorganic salts in feed solution may quench the small portion of •OH radicals [55].

These above results exhibited that heterojunction photocatalysts can effectively enhance photocatalytic activity and improve the charge recombination rate [53,54]. The achievable enhancement by increasing the BMCN65 loading onto the PVDF nanofiber will be determined in the next section.

3.3. BMCN65 loading onto PVDF fiber composite membrane

When the photocatalyst loading increased, the photodegradation performance was expected to be enhanced due to more ROS being generated on the photocatalyst surface. However, excess photocatalysts can interfere with the light transmittance and hence deteriorate the photodegradation efficiency [56]. Loadings were investigated from 0.25 to 1.75 mg.cm^{-2}.

PVDF-BMCN65 CNM with different BMCN65 loadings achieved saturation and the mass adsorbed (m_{ads}) increased from $1{\cdot}10^{-3}$ to $6{\cdot}10^{-3}$ ng.cm^{-2} with increased BMCN65 loading (Fig. S16C). This phenomenon was attributed to the increased loading providing more active adsorption sites (e.g. amino groups and π-π conjugated aromatic rings of CN) for secondary interactions (e.g. hydrogen bonding, Van Der Waal interaction, and π-π interaction) [57]. Fig. 7 showed that the PVDF-BMCN65 NCM had a removal of around 70 ± 7 % at the loading of 0.25 mg.cm^{-2}. When the loading exceeds 1 mg.cm^{-2}, removal decreased to 54 ± 7 % at 1.25 mg.cm^{-2}. The apparent rate of disappearance r'' followed the same trend as E2 removal in that r'' decreased from $(4.84 \pm 0.6){\cdot}10^{11}$ mol.m^{-2}.s^{-1} to $(3.76 \pm 0.7){\cdot}10^{11}$ mol.m^{-2}.s^{-1} at a loading of 1.25 mg.cm^{-2}. Two possible reasons can explain this phenomenon; firstly the self-aggregation of catalysts, which decreased photocatalytic activity [58], and secondly, the contact area of the same thickness between the photocatalytic membrane and micropollutants remained constant. Once the photocatalyst loading reached a certain value, the excessive catalyst hindered the contact area between micropollutants and the photocatalytic membrane [59], as well as light penetration. To gain deeper insight, the different BMCN65 loadings were investigated by SEM and light transmission. Excessive loading above 1 mg.cm^{-2} caused the self-aggregation of BMCN65 (Fig. S5) and the reduction in light transmission with increasing BMCN65 loading (Fig. S12), which limited the amount of effective reactive sites and decreased the photodegradation efficiency. Loading experiments for BMCN65 were verified with methylene blue (c_f = 1 mg.L^{-1}, Fig. S21), wherein 1 mg.cm^{-2} loading exhibits the highest removal efficiency (R = 24 ± 7 %).

According to the photocatalyst limitations, optical properties, photocatalyst ratio, and loading of photocatalytic nanomaterials significantly influenced E2 removal. A PVDF-BMCN65 NCM with a loading of 1 mg.cm^{-2} was selected for subsequent experiments to investigate environmental factors affecting photocatalytic degradation. These parameters included operating conditions and solution chemistry, which were critical for guiding further development of PMRs for environmental application.

3.4. Water flux and hydraulic residence time

The hydraulic residence time ($\bar{t}$) corresponded to the residence time between micropollutants and the photocatalytic membrane surface without considering adsorption. Adjusted with water flux, $\bar{t}$ was a limiting factor for photodegradation performance and can be calculated from **Eq.S3** using permeate flow rate and membrane porosity. Meanwhile, molar flux, which influenced the amount of the micropollutant available on the photocatalytic membrane surface, can be calculated using **Eq.S6** from water flux and micropollutant concentration. This section investigated fluxes with various water flux, ranging from 60 to 3000 L.m^{-2}.h^{-1} (flow rate from 0.2 to 10 mL.min^{-1}) with corresponding $\bar{t}$ between 1.57 s and 0.03 s, while the E2 molar flux increased from $0.6{\cdot}10^{-11}$ to $31{\cdot}10^{-11}$ mol.m^{-2}.s^{-1} (Fig. 8.).

PVDF-BMCN65 NCM reached saturation with varying water fluxes, while the mass adsorbed (m_{ads}) decreased from $6{\cdot}10^{-3}$ to $0.4{\cdot}10^{-3}$ ng.cm^{-2} with increasing water flux (Fig. S16E). A decline in E2 removal can be observed from 93 ± 3 to 50 ± 8 % (from 60 to 3000 L.m^{-2}.h^{-1}), while r'' increased from $(0.7 \pm 0.3){\cdot}10^{-11}$ to $(17 \pm 1.8){\cdot}10^{-11}$ mol.m^{-2}.s^{-1}. The reduced removal was attributed to the shortened contact time between micropollutants and the photocatalytic membrane surface [60]. Moreover, r'' exhibited an opposite trend to E2 removal, because the photodegradation process was in the mass-transfer controlled regime [61]. A strong linear correlation (R^2 = 0.99) was observed when

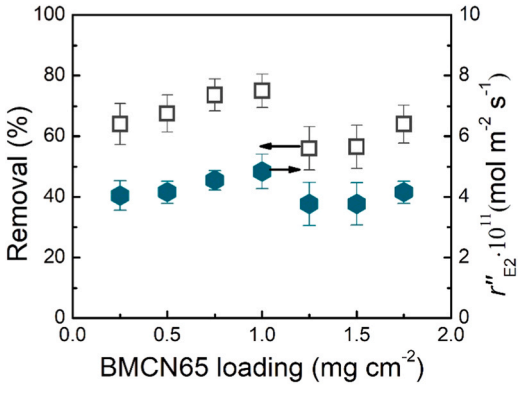

Fig. 7. E2 removal and rate of disappearance as function of BMCN65 loading (PVDF-BMCN65 NCM, irradiance 8 mW.cm^{-2} (350 - 1150 nm), flux 600 L.m^{-2}.h^{-1}, flow rate 2 mL.min^{-1}, pH 8.2 ± 0.4, 24 ± 2 °C, E2 concentration 100 ng.L^{-1}, 1 mM $NaHCO_3$, 10 mM NaCl, 27.2 mg.L^{-1} EtOH, 79.2 mg.L^{-1} MeOH).

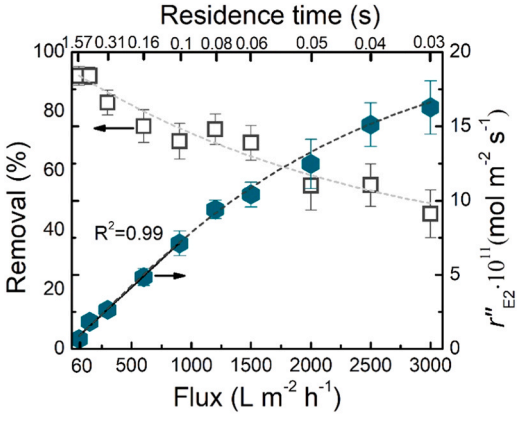

Fig. 8. E2 removal and rate of disappearance as a function of flux (PVDF-BMCN65 NCM, M_{PC}: 1 mg.cm^{-2}, irradiance 8 mW.cm^{-2} (350 - 1150 nm), pH 8.2 ± 0.4, 24 ± 2 °C, E2 concentration 100 ng.L^{-1}, 1 mM $NaHCO_3$, 10 mM NaCl, 27.2 mg.L^{-1} EtOH, 79.2 mg.L^{-1} MeOH).

$\bar{t}$ decreased from 1.57 to 0.1 s (water flux from 60 to 900 L.m^{-2}.h^{-1}), indicating that the photocatalytic degradation kinetics were in the mass-transfer-controlled regime at $\bar{t} > 0.1$ s. These results indicated that molar flux and mass transfer of E2 molecules to the photocatalytic membrane surface dominated photodegradation efficiency in the flow-through PMR [62]. When $\bar{t} < 0.1$ s (water flux > 900 L.m^{-2}.h^{-1}), the rate of disappearance reached a plateau, indicating that photodegradation degradation kinetics were no longer diffusion-limited and achieve a surface-reaction-controlled regime [63].

In this section, the hydraulic residence time ($\bar{t}$) was the rate-controlling step for the mass-transfer-controlled and surface-reaction-controlled regimes during heterogeneous photocatalysis, which was an observation similar to the phenomenon in other flow-through PMRs over an immobilized photocatalyst [64]. Thus, a flux of 600 L.m^{-2}.h^{-1} was chosen for other experiments because it balanced the small influence of mass transfer under 900 L.m^{-2}.h^{-1} and provided a fair compromise between E2 removal and rate of disappearance (r'').

3.5. Solar simulator light intensity

Light intensity can be defined as the number of photons generated per unit of area in the PMR. Higher light intensity can yield more photons from light resources, and a photocatalyst absorbing more photons can generate a higher ROS concentration [65]. The experiments with various light intensities were investigated from 8 to 100 mW.cm^{-2}.

Two regimes of light intensity effects on photodegradation can be observed in Fig. 9. When the solar simulator light was off, E2 removal was zero, indicating that the photocatalytic membrane cannot remove E2 without light activation. When the solar simulator turned on, E2 removal exhibited 75 ± 7 % at the low irradiance of 8 mW.cm^{-2}. With increasing light intensity, E2 removal increased to 91 ± 3 %, attributed to an improved charge recombination rate at high light irradiation [66]. Moreover, r'' increased from $4.84 \pm 0.6 \cdot 10^{11}$ to $5.89 \pm 0.3 \cdot 10^{11}$ mol.m^{-2}s^{-1}. This observation was similar to what Herrmann *et al.* [65] demonstrated when the reaction rate followed the first-order kinetic (α value = 1) at low light intensity, whereas at moderate light intensity, the reaction rate reached a leveled-off state (α value = 0.5). Moreover, the reaction rate became constant at a sufficiently high light intensity, where kinetics was only limited by mass transfer.

In this section, light intensity exhibited a slightly positive correlation with E2 removal and the rate of disappearance, indicating that reaction kinetics didn't reach the mass-transfer-limited regime. Hence, a light intensity of 8 mW.cm^{-2} was employed for investigating other water quality parameters. Solution chemistry will be explored in the next section.

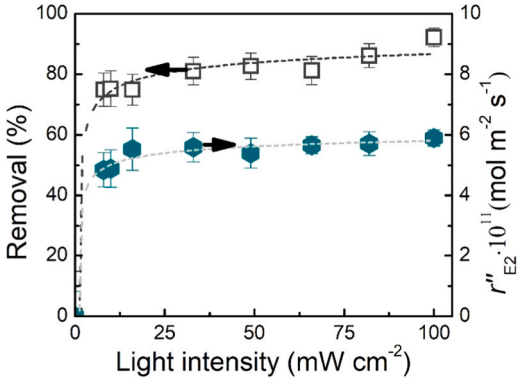

Fig. 9. E2 removal and rate of disappearance as a function of light intensity (PVDF-BMCN65 NCM, loading 1 mg.cm^{-2}, irradiance (350 - 1150 nm), flux 600 L.m^{-2}.h^{-1}, flow rate 2 mL.min^{-1}, pH 8.2 ± 0.4, 24 ± 2 °C, E2 concentration 100 ng.L^{-1}, 1 mM $NaHCO_3$, 10 mM NaCl, 27.2 mg.L^{-1} EtOH, 79.2 mg.L^{-1} MeOH).

3.6. Initial steroid hormone concentration

During the photodegradation experiment, the initial SH concentration determined the number of SH molecules present in the NCM. The experiments involved investigating various initial E2 concentrations, ranging from 0.05 to 1000 μg.L^{-1}, which ranges from very low environmental concentrations to near the solubility limit in water (E2 solubility is 1.7–3.9 mg.L^{-1} (20–25 °C) [67]).

Saturation of the PVDF-BMCN65 NCM was reached with various initial concentrations in the dark phase, and the mass adsorbed (m_{ads}) increased from $1.5 \cdot 10^{-3}$ to 21 ng.cm^{-2} in response to the increasing initial concentration (Fig. S16G). Fig. 10 illustrated two regimes of the effects of the initial concentration on photocatalytic degradation. For the initial concentrations from 0.05 to 10 μg.L^{-1}, E2 removal exhibited moderate efficiency (R = 60–80 %) with a perfect linear correlation (R^2 =0.999) of r'', which can also be observed at low E2 concentrations. This indicated that the photodegradation kinetic follows apparent first-order kinetics (following the Langmuir-Hinshelwood model, L-H model). Typically, the L-H model can be separated with correlation (R^2) into zero-order kinetic (R^2 >1), first-order kinetic (1 ≧R^2 >0.9), and second-order kinetic (R^2 <0.9) [68]. At higher E2 concentrations (>10 μg.L^{-1}), E2 removal dramatically decreased from 75 ± 7 to 14 ± 11 %, while r'' increased from $4.84 \pm 0.6 \cdot 10^{11}$ to $6.48 \pm 0.7 \cdot 10^{8}$ mol.m^{-2}s^{-1}. This was attributed to the membrane saturation with E2 molecules and possibly by-products, which result in an apparent reduction in kinetics and a transition to a zero-order kinetic [69]. Simultaneously, there appears to be an insufficient amount of ROS produced to degrade micropollutants.

These results showed that increasing the initial feed concentration can improve contact between micropollutants and the photocatalytic membrane surface, leading to an enhanced rate of r'' during photodegradation. Nevertheless, the concentration of SHs in environmental water resources was below the physiological level (sub-ng.L^{-1}) [1,2]. Thus, the environmentally relevant concentration (100 ng.L^{-1}) was used to investigate the various pH and SH types.

3.7. Feed solution pH

The pH of feed solution influenced the surface charge of the catalyst

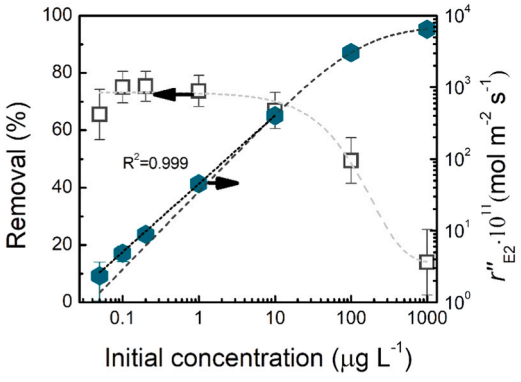

Fig. 10. E2 removal and rate of disappearance as a function of initial E2 concentration (PVDF-BMCN65 NCM, M_{PC}: 1 mg.cm^{-2}, irradiance 8 mW.cm^{-2} (350 - 1150 nm), flux 600 L.m^{-2}.h^{-1}, flow rate 2 mL.min^{-1}, pH 8.2 ± 0.4, 24 ± 2 °C, 1 mM $NaHCO_3$, 10 mM NaCl, 27.2 mg.L^{-1} EtOH, 79.2 mg.L^{-1} MeOH.).

and micropollutants, which can cause either charge repulsion or adsorption [10]. Xu *et al.* [70] reported that ROS production increased with increasing pH values because the high OH^- concentration can enhance $^{\bullet}OH$ formation in the alkaline solution via the redox reaction ($E_{OH^-/^{\bullet}OH}$= 2.38 V vs NHE). Thus, the photodegradation performance of E2 on the PVDF-BMCN65 NCM was studied at various pH values from 2 to 12.

PVDF-BMCN65 NCM reached saturation irrespective of feed solution pH (Fig. S16D). The mass adsorbed (m_{ads}) decreased from $6.1{\cdot}10^{-3}$ to $3.4{\cdot}10^{-3}$ ng.cm^{-2} with increasing pH. Zhu *et al.* [71] determined the surface functional group of CN at various pH values using FT-IR spectra, thus indicating that the protonation of the amine group at acidic conditions can enhance micropollutants adsorption (e.g., hydrogen bonding and π-π interaction). Fig. 11 revealed that the removal efficiency remained relatively constant between pH 2–6 (R= 84 ± 4 %) and decreased somewhat above pH 6 (67 ± 7 % for pH 12). Moreover, r''followed the same trend and decreased from $6.1 \pm 0.3{\cdot}10^{-11}$ to $3.1 \pm 7.2{\cdot}10^{-11}$ mol.m^{-2}.s^{-1} as pH increased from 6 to 12. Due to the pK_a range of E2 (pK_a = 10.2–10.7 [72]) and the pH_{IEP} of PVDF-BMCN65 NCM (pH_{IEP} = 5), the catalyst surface exhibited a negative surface charge and E2 was dissociated above pH 10.2–10.7. At pH < 8.2, a slight increase in both E2 removal and r'' was observed, which can be attributed to the improvement of E2 adsorption onto the photocatalytic membrane surface. Hence, the charge repulsion above pH 8.2 caused a reduction in E2 removal efficiency [10].

In summary, it can be observed that as pH increases, photodegradation efficiency decreased slightly due to reduced E2 adsorption and charge repulsion between the BMCN65 surface and E2 molecules. The WHO guidelines indicated that the pH of drinking water ranged from 6.5 to 8.5 [73]. Thus, a pH of about 8 was used for investigating the various steroid hormone types.

3.8. Steroid hormone type

The chemical structure of steroid hormones can impact the SH photodegradation performance. Yost *et al.* reported the list of SH activities (a), in which the order was E2 (a=1)>E1 (a=0.02–0.45)> P (a=$2{\cdot}10^{-2}$)> T (a=<$1{\cdot}10^{-2}$) determined through the YES (Yeast Estrogen Screen) assay with E2 as the reference compound [74,75]. Molecule reactivity can be examined by the Frontier Electron Theory (FET), in which electrophiles can rapidly and non-selectively attack electron-rich sites (e.g., aromatic ring) [76,77]. The different SHs (E1, E2, P, and T) were investigated in the same initial concentration.

Fig. 12 showed that E1 and E2 had a moderate removal (R = 60–75 %) compared to P and T (R = 22–45 %). Meanwhile, r'' followed the same trend as SH removal with the order E2 > E1 > T > P. During the photodegradation process, the free radical can serve as the electrophile to degrade the phenolic chemicals (E1 and E2) quickly. For the possible degradation pathway, Qing *et al.* [78] reported that the carbon/aromatic rings of E2 molecules were hydroxylated or replaced by the -OH group to form three different intermediates in the beginning. Subsequently, aromatic rings of intermediates were attacked by $^{\bullet}OH$ and $^{\bullet}O_2^-$, and then converted into small intermediates, CO_2 and H_2O by hydroxylation, ring cleavage, and decarboxylation. Meanwhile, Ali *et al.* [79] reported that the degradation pathway of E1 confirmed that $^{\bullet}OH$ and $^{\bullet}O_2^-$ can easily attack the aromatic ring to decompose molecules, which is similar to the degradation pathway of E2. Even though the chemical structure of T and P was without the aromatic ring, the YES assay and calculated FET for SHs type indicated that the P and T activity were lower than E1 and E2. Hence, the photodegradation performance of P and T exhibits low removal efficiency [74,75,80]. Furthermore, Qing *et al.* [78] used Ecological Structure Activity Relationships (ECOSAR) Predictive Model to evaluate the biotoxicity. The acute and chronic toxicity based on intermediates and E2 decreased with the photodegradation process.

3.9. Removal of 17β-estradiol at optimized conditions

To investigate whether the PVDF-BMCN65 NCM can meet the WHO guideline of 1 ng.L^{-1} for 17β-estradiol in drinking water, the photodegradation performance was optimized based on the results obtained above for a final experiment.

At optimized conditions a 3.6 ± 2.5 ng.L^{-1} E2 permeate concentration near the detection limit was achieved for the single-pass dead-end filtration at 60 L.m^{-2}.h^{-1} and 100 mW.cm^{-2} with the PVDF-BMCN65 NCM (catalyst loading 1 mg.cm^{-2}). Despite the analytical method being insufficient for E2 (LOQ = 3.8 ng.L^{-1} [81]) to reach the 1 ng.L^{-1} guideline value, this optimized result, clearly demonstrates the significant potential of photocatalytic membrane treatment for removing SHs from water. The specific energy consumption was not calculated for such a very small laboratory system, although energy savings from the permeability increase compared to dense membranes implies that the process should be feasible if efficient light sources are implemented. This requires validation at pilot scale.

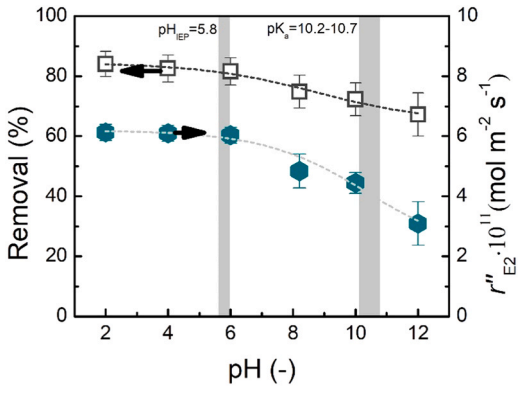

Fig. 11. E2 removal and rate of disappearance as a function of pH (2–12) (PVDF-BMCN65 NCM, loading 1 mg.cm^{-2}, irradiance 8 mW.cm^{-2} (350 - 1150 nm), flux 600 L.m^{-2}.h^{-1}, flow rate 2 mL.min^{-1}, 24 ± 2 °C, c_f: 100 ng.L^{-1}, 1 mM $NaHCO_3$, 10 mM NaCl, 27.2 mg.L^{-1} EtOH, 79.2 mg.L^{-1} MeOH.).

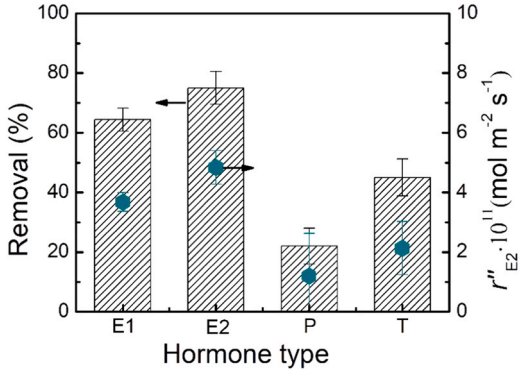

Fig. 12. E2 removal and rate of disappearance as a function of hormone type (PVDF-BMCN65 NCM, loading 1 mg.cm^{-2}, irradiance 8 mW.cm^{-2} (350 - 1150 nm), flux 600 L.m^{-2}.h^{-1}, flow rate 2 mL.min^{-1}, pH 8.2 ± 0.4, 24 ± 2 °C, SH concentration 100 ng.L^{-1}, 1 mM $NaHCO_3$, 10 mM NaCl, 27.2 mg.L^{-1} EtOH, 79.2 mg.L^{-1} MeOH.).

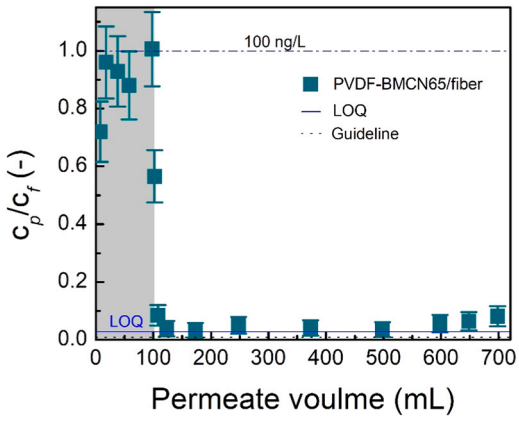

Fig. 13. c_p/c_f of PVDF-BMCN65 NCM as a function of permeate volume (loading 1 mg.cm^{-2}, irradiance 100 mW.cm^{-2} (350 - 1150 nm), flux 60 L.m^{-2}.h^{-1}, flow rate 0.2 mL.min^{-1}, 24 ± 2 °C, E2 concentration 100 ng.L^{-1}, 1 mM $NaHCO_3$, 10 mM NaCl, 27.2 mg.L^{-1} EtOH, 79.2 mg.L^{-1} MeOH).

Additional examples of photocatalytic membranes and their performance on micropollutant removal are detailed in Table S11. Most of these studies utilized a solar simulator, Xe lamp, UV lamp and LED lamp as a light source with the removal ranging from 22 to 98 %. In this systems a solar simulator was used to irradiate PVDF-BMCN65 NCM for the E2 photodegradation at environmentally relevant concentrations (100 ng.L^{-1}). This result highlights that PVDF-BMCN65 NCM can effectively photodegrade E2. Furthermore, this enhanced efficiency underscored their potential for wastewater treatment processes.

4. Conclusions

The photodegradation of SHs using PVDF-BMCN65 NCM in a flow-through single-pass PMR was evaluated for SHs removal under solar simulator irradiation. The in-depth investigations quantified the environmental factors at environmentally relevant SH concentrations (100 ng.L^{-1}). The most significant limitation were the photocatalyst properties, in which PVDF-BMCN65 NCM exhibited excellent photodegradation performance due to the improvement of longer photon lifetime, broadened wavelength absorption, charge recombination rate, and morphology (no self-aggregation) of the photocatalyst.

Under the chosen operating conditions, the hydraulic residence time was found to be an important limiting factor for E2 removal and rate of disappearance. At flux values below 900 L.m^{-2}.h^{-1}, r'' exhibited a linear increasement, which indicated photodegradation kinetics controlled by the molar flux. Moreover, the light intensity slightly improved the E2 removal and r'', which was attributed to the improvement of the charge recombination rate.

In terms of water chemistry, the removal performance was inhibited to some extent in an alkaline solution due to decreased E2 adsorption onto a photocatalytic membrane surface via charge repulsion. Meanwhile, the experiments with different SH types exhibited moderate removal efficiency of E1 and E2 (R=60–75 %) at a water flux of 600 L m^{-2}.h^{-1} ($\bar{t}$ = 0.16 s). At optimized conditions, E2 removal was higher than 96 % at an environmentally relevant feed concentration (100 ng.L^{-1}), a flux of 60 L.m^{-2}.h^{-1}, 100 mW.cm^{-2}, and BMCN65 1 mg.cm^{-2}.

This study confirmed that heterojunction photocatalysts in the PMR can enhance the photocatalytic degradation of micropollutants. Furthermore, developing the nanoconfined heterojunction photocatalyst (particle size in 10–30 nm) maybe the most promising strategy to further enhance SH removal efficiency at environmentally relevant concentrations in the PMR system.

CRediT authorship contribution statement

Zhi-Fu Lin: Writing – original draft, Visualization, Validation, Methodology, Investigation, Formal analysis, Data curation, Conceptualization. **Han-Ya Lin:** Writing – review & editing, Validation, Methodology, Investigation, Data curation, Conceptualization. **Ruey-An Doong:** Writing – review & editing, Validation, Supervision, Resources, Project administration, Methodology, Funding acquisition, Conceptualization. **Andrea I. Schaefer:** Writing – review & editing, Validation, Supervision, Resources, Project administration, Methodology, Funding acquisition, Conceptualization.

Environmental Implications

Steroid hormone micropollutant are abundant in effluents and pose a threat to environment and health. Removal from water is a global challenge. Membrane photocatalysis is an effective emerging technology that can degrade such micropollutants in situ. A poly(vinylidene fluoride) (PVDF) nanofiber composite membrane (NCM) with immobilized visible-light-responsive g-C_3N_4/Bi_2MoO_6 (BMCN) was investigated. Significantly enhanced performance of steroid hormone degradation was observed in terms of utilization of sunlight. Up to 96 % of degradation was achieved with hydraulic residence times in the order of seconds. This results in both high removal of micropollutants and potentially significant energy savings through the use of sunlight.

Declaration of Competing Interest

The authors declare that they have no known competing financial interests or personal relationships that could have appeared to influence the work reported in this paper.

Data Availability

Data will be made available on request.

Acknowledgments

The National Science and Technology Council (NSTC), Taiwan-Deutscher Akademischer Austauschdienst (DAAD), Germany Project-based Personnel Exchange Program funding 2021–2024 enabled this collaboration for financial support under Grant nos. DAAD 57678889, NSTC 110-2927-I-007-510 and NSTC 111-2927-I-007-501. Helmholtz Association is acknowledged for providing KIT-IAMT funding through the recruitment initiative. Dr. Siqi Liu performed the UHPLC analysis. Millipore was thanked for supplying the support membranes. Solvay S. A. provided the PVDF powder. Dr. Joachim Binder and Monika Raab (IAM, KIT) are thanked for operating mercury intrusion porosimetry and discussion of results. The Instrumentation Resource Center at NTHU (Taiwan) contributed to SEM, EPR, and time-resolved PL measurement analysis. Instrumentation Resource Center at NCTU (Taiwan) is thanked for UPS analysis.

Supporting information

Supporting information includes: 1). Equation table (Table S1); 2). Experiment protocol (Table S2); 3) Summary of experimental parameters (Table S3); 4) 4. Real images of experimental setup and PVDF-BMCN65 NCM (Fig. S1); 5)Membrane characterization: 5.1) X-ray diffraction (Fig. S2), 5.2) Fourier transform infrared spectroscopy (Fig. S3), 5.3) X-ray photoelectron spectroscopy (Fig. S4), 5.4) Morphology (Fig. S5), 5.5) Zeta potential (Fig. S6), 5.6) UV/Visible absorbance spectrum and diffuse reflectance spectrum (Fig. S7), 5.7)

Photon life (Fig. S8), 5.8) Photoelectrochemical analysis (Fig. S9), 5.9) Band structure (Fig. S10), 5.10) Electron paramagnetic resonance (Fig. S11), 5.11) Light transmittance affects the BMCN65 loading (Fig. S12), 5.12) Permeability variation with BMCN65 loading (Fig. S13), 5.13) The loss of BMCN65 loading after experiment (Fig. S14); 6) Absorption spectrum for solar simulator (Fig. S15); 7) Normalized parameters in each experiment (Fig. S16-19); 8) Methylene blue experiments through PVDF-BMCN NCM (Fig. S20-21); 9) Error estimation (Table S7); 10) Membrane porosity (Table S8); 11) Theoretical calculation (Table S9-10); 12) Comparison photocatalytic membrane (Table S11);.

Appendix A. Supporting information

Supplementary data associated with this article can be found in the online version at doi:10.1016/j.jhazmat.2024.134765.

References

[1] Petrie, B., Barden, R., Kasprzyk-Hordern, B., 2015. A review on emerging contaminants in wastewaters and the environment: current knowledge, understudied areas and recommendations for future monitoring. Water Res 72, 3–27.

[2] Khan, N.A., Khan, S.U., Ahmed, S., Farooqi, I.H., Yousefi, M., Mohammadi, A.A., Changani, F., 2020. Recent trends in disposal and treatment technologies of emerging-pollutants- a critical review. TrAC Trends Anal Chem 122.

[3] Rout, P.R., Zhang, T.C., Bhunia, P., Surampalli, R.Y., 2021. Treatment technologies for emerging contaminants in wastewater treatment plants: a review. Sci Total Environ 753, 141990.

[4] Schulze, S., Zahn, D., Montes, R., Rodil, R., Quintana, J.B., Knepper, T.P., Reemtsma, T., Berger, U., 2019. Occurrence of emerging persistent and mobile organic contaminants in European water samples. Water Res 153, 80–90.

[5] Metcalfe, C.D., Bayen, S., Desrosiers, M., Munoz, G., Sauve, S., Yargeau, V., 2022. An introduction to the sources, fate, occurrence and effects of endocrine disrupting chemicals released into the environment. Environ Res 207, 112658.

[6] Kase, R., Javurkova, B., Simon, E., Swart, K., Buchinger, S., Könemann, S., Escher, B.I., Carere, M., Dulio, V., Ait-Aissa, S., Hollert, H., Valsecchi, S., Polesello, S., Behnisch, P., di Paolo, C., Olbrich, D., Sychrova, E., Gundlach, M., Schlichting, R., Leborgne, L., Clara, M., Scheffknecht, C., Marneffe, Y., Chalon, C., Tusil, P., Soldan, P., von Danwitz, B., Schwaiger, J., Palao, A.M., Bersani, F., Perceval, O., Kienle, C., Vermeirssen, E., Hilscherova, K., Reifferscheid, G., Werner, I., 2018. Screening and risk management solutions for steroidal estrogens in surface and wastewater. TrAC Trends Anal Chem 102, 343–358.

[7] Bhatt, P., Bhandari, G., Bilal, M., 2022. Occurrence, toxicity impacts and mitigation of emerging micropollutants in the aquatic environments: recent tendencies and perspectives. J Environ Chem Eng 10.

[8] Ghazal, H., Koumaki, E., Hoslett, J., Malamis, S., Katsou, E., Barcelo, D., Jouhara, H., 2022. Insights into current physical, chemical and hybrid technologies used for the treatment of wastewater contaminated with pharmaceuticals. J Clean Prod 361.

[9] Leong, S., Razmjou, A., Wang, K., Hapgood, K., Zhang, X., Wang, H., 2014. TiO_2 based photocatalytic membranes: a review. J Membr Sci 472, 167–184.

[10] Mozia, S., 2010. Photocatalytic membrane reactors (PMRs) in water and wastewater treatment. A Rev Sep Purif Technol 73, 71–91.

[11] Constantino, D.S.M., Dias, M.M., Silva, A.M.T., Faria, J.L., Silva, C.G., 2022. Intensification strategies for improving the performance of photocatalytic processes: a review. J Clean Prod 340.

[12] Janssens, R., Mandal, M.K., Dubey, K.K., Luis, P., 2017. Slurry photocatalytic membrane reactor technology for removal of pharmaceutical compounds from wastewater: towards cytostatic drug elimination. Sci Total Environ 599-600, 612–626.

[13] Rengifo-Herrera, J.A., Pulgarin, C., 2023. Why five decades of massive research on heterogeneous photocatalysis, especially on TiO_2, has not yet driven to water disinfection and detoxification applications? Critical review of drawbacks and challenges. Chem Eng J 477.

[14] Yin, J., Deng, B., 2015. Polymer-matrix nanocomposite membranes for water treatment. J Membr Sci 479, 256–275.

[15] Hodges, B.C., Cates, E.L., Kim, J.H., 2018. Challenges and prospects of advanced oxidation water treatment processes using catalytic nanomaterials. Nat Nanotechnol 13, 642–650.

[16] Zhang, M., Yang, Y., An, X., Hou, L.-a, 2021. A critical review of g-C_3N_4-based photocatalytic membrane for water purification. Chem Eng J 412.

[17] Argurio, P., Fontananova, E., Molinari, R., Drioli, E., 2018. Photocatalytic membranes in photocatalytic membrane reactors. Processes 6.

[18] Low, J., Yu, J., Jaroniec, M., Wageh, S., Al-Ghamdi, A.A., 2017. Heterojunction photocatalysts. Adv Mater 29.

[19] Liu, X., Gu, S., Zhao, Y., Zhou, G., Li, W., 2020. $BiVO_4$, Bi_2WO_6 and Bi_2MoO_6 photocatalysis: a brief review. J Mater Sci Technol 56, 45–68.

[20] Wang, Y., Gao, B., Yue, Q., Wang, Z., 2020. Graphitic carbon nitride (g-C_3N_4)-based membranes for advanced separation. J Mater Chem A 8, 19133–19155.

[21] Kallawar, G.A., Barai, D.P., Bhanvase, B.A., 2021. Bismuth titanate based photocatalysts for degradation of persistent organic compounds in wastewater: a comprehensive review on synthesis methods, performance as photocatalyst and challenges. J Clean Prod 318.

[22] Bai, L., Huang, H., Yu, S., Zhang, D., Huang, H., Zhang, Y., 2022. Role of transition metal oxides in g-C_3N_4-based heterojunctions for photocatalysis and supercapacitors. J Energy Chem 64, 214–235.

[23] Yang, H., 2021. A short review on heterojunction photocatalysts: carrier transfer behavior and photocatalytic mechanisms. Mater Res Bull 142.

[24] Parul, Kaur, K., Badru, R., Singh, P.P., Kaushal, S., 2020. Photodegradation of organic pollutants using heterojunctions: a review. J Environ Chem Eng 8.

[25] Li, H., Liu, J., Hou, W., Du, N., Zhang, R., Tao, X., 2014. Synthesis and characterization of g-C_3N_4/Bi_2MoO_6 heterojunctions with enhanced visible light photocatalytic activity. Appl Catal B: Environ 160-161, 89–97.

[26] Liu, W., Zhou, J., Zhou, Y., Liu, D., 2021. Peroxymonosulfate-assisted g-C_3N_4@Bi_2MoO_6 photocatalytic system for degradation of nimesulide through phenyl ether bond cleavage under visible light irradiation. Sep Purif Technol 264.

[27] Cui, Y., Yang, L., Zheng, J., Wang, Z., Li, B., Yan, Y., Meng, M., 2021. Synergistic interaction of Z-scheme 2D/3D g-C_3N_4/BiOI heterojunction and porous PVDF membrane for greatly improving the photodegradation efficiency of tetracycline. J Colloid Interface Sci 586, 335–348.

[28] Jiménez-Bautista, K., Gascó, A., Ramos, D.R., Palomo, E., Muelas-Ramos, V., Canle, M., Hermosilla, D., Bahamonde, A., 2023. Solar-assisted photodegradation of pesticides over pellet-shaped TiO_2-kaolin catalytic macrocomposites at semi-pilot-plant scale: elucidation of photo-mechanisms and water matrix effect. J Clean Prod 426.

[29] Kundu, S., Karak, N., 2022. Polymeric photocatalytic membrane: an emerging solution for environmental remediation. Chem Eng J 438.

[30] Li, N., Lu, X., He, M., Duan, X., Yan, B., Chen, G., Wang, S., 2021. Catalytic membrane-based oxidation-filtration systems for organic wastewater purification: a review. J Hazard Mater 414, 125478.

[31] Qing, W., Li, X., Shao, S., Shi, X., Wang, J., Feng, Y., Zhang, W., Zhang, W., 2019. Polymeric catalytically active membranes for reaction-separation coupling: a review. J Membr Sci 583, 118–138.

[32] Huang, J., Hu, J., Shi, Y., Zeng, G., Cheng, W., Yu, H., Gu, Y., Shi, L., Yi, K., 2019. Evaluation of self-cleaning and photocatalytic properties of modified g-C_3N_4 based PVDF membranes driven by visible light. J Colloid Interface Sci 541, 356–366.

[33] Qing, W., Wu, J., Chen, N., Liu, L., Deng, Y., Zhang, W., 2017. A genuine in-situ water removal at a molecular lever by an enhanced esterification-pervaporation coupling in a catalytically active membrane reactor. Chem Eng J 323, 434–443.

[34] Peters, T.A., Benes, N.E., Keurentjes, J.T.F., 2007. Preparation of Amberlyst-coated pervaporation membranes and their application in the esterification of acetic acid and butanol. Appl Catal A: Gen 317, 113–119.

[35] Bedford, N.M., Steckl, A.J., 2010. Photocatalytic self cleaning textile fibers by coaxial electrospinning. ACS Appl Mater Interfaces 2, 2448–2455.

[36] Wang, S., Wang, L., Cong, H., Wang, R., Yang, J., Li, X., Zhao, Y., Wang, H., 2022. A review: g-C_3N_4 as a new membrane material. J Environ Chem Eng 10.

[37] Park, M., Ko, Y.T., Ji, M., Cho, J.S., Wang, D.H., Lee, Y.-I., 2022. Facile self-assembly-based fabrication of a polyvinylidene fluoride nanofiber membrane with immobilized titanium dioxide nanoparticles for dye wastewater treatment. J Clean Prod 378.

[38] Chin, S.S., Chiang, K., Fane, A.G., 2006. The stability of polymeric membranes in a TiO_2 photocatalysis process. J Membr Sci 275, 202–211.

[39] Riaz, S., Park, S.-J., 2020. An overview of TiO_2-based photocatalytic membrane reactors for water and wastewater treatments. J Ind Eng Chem 84, 23–41.

[40] Kang, G.-d, Cao, Y.-m, 2014. Application and modification of poly(vinylidene fluoride) (PVDF) membranes – a review. J Membr Sci 463, 145–165.

[41] Shi, Z., Zhang, Y., Liu, T., Cao, W., Zhang, L., Li, M., Chen, Z., 2020. Synthesis of BiOBr/Ag_3PO_4 heterojunctions on carbon-fiber cloth as filter-membrane-shaped photocatalyst for treating the flowing antibiotic wastewater. J Colloid Interface Sci 575, 183–193.

[42] Sarkodie, B., Amesimeku, J., Frimpong, C., Howard, E.K., Feng, Q., Xu, Z., 2023. Photocatalytic degradation of dyes by novel electrospun nanofibers: a review. Chemosphere 313, 137654.

[43] Yang, J., Song, H., Xu, O., Wan, S., Zhu, X., 2022. Preparation of g-C_3N_4@bismuth dihalide oxide heterojunction membrane and its visible light catalytic performance. Appl Surf Sci 583.

[44] Ramasundaram, S., Son, A., Seid, M.G., Shim, S., Lee, S.H., Chung, Y.C., Lee, C., Lee, J., Hong, S.W., 2015. Photocatalytic applications of paper-like poly(vinylidene fluoride)-titanium dioxide hybrids fabricated using a combination of electrospinning and electrospraying. J Hazard Mater 285, 267–276.

[45] Liu, L., Liu, Z., Bai, H., Sun, D.D., 2012. Concurrent filtration and solar photocatalytic disinfection/degradation using high-performance Ag/TiO_2 nanofiber membrane. Water Res 46, 1101–1112.

[46] Lotfi, S., Fischer, K., Schulze, A., Schafer, A.I., 2022. Photocatalytic degradation of steroid hormone micropollutants by TiO_2-coated polyethersulfone membranes in a continuous flow-through process. Nat Nanotechnol 17, 417–423.

[47] Lyubimenko, R., Gutierrez Cardenas, O.I., Turshatov, A., Richards, B.S., Schäfer, A. I., 2021. Photodegradation of steroid-hormone micropollutants in a flow-through membrane reactor coated with Pd(II)-porphyrin. Appl Catal B: Environ 291.

[48] Wang, L., Lan, X., Peng, W., Wang, Z., 2021. Uncertainty and misinterpretation over identification, quantification and transformation of reactive species generated in catalytic oxidation processes: a review. J Hazard Mater 408, 124436.

[49] Dang, V.D., Adorna, J., Annadurai, T., Bui, T.A.N., Tran, H.L., Lin, L.-Y., Doong, R.-A., 2021. Indirect Z-scheme nitrogen-doped carbon dot decorated Bi_2MoO_6/g-C_3N_4

photocatalyst for enhanced visible-light-driven degradation of ciprofloxacin. Chem Eng J 422.
[50] Berger, T.E., Regmi, C., Schäfer, A.I., Richards, B.S., 2020. Photocatalytic degradation of organic dye via atomic layer deposited TiO_2 on ceramic membranes in single-pass flow-through operation. J Membr Sci 604.
[51] Liu, S., Veron, E., Lotfi, S., Fischer, K., Schulze, A., Schafer, A.I., 2023. Poly (vinylidene fluoride) membrane with immobilized TiO_2 for degradation of steroid hormone micropollutants in a photocatalytic membrane reactor. J Hazard Mater 447, 130832.
[52] Preethi, L.K., Mathews, T., Nand, M., Jha, S.N., Gopinath, C.S., Dash, S., 2017. Band alignment and charge transfer pathway in three phase anatase-rutile-brookite TiO_2 nanotubes: an efficient photocatalyst for water splitting. Appl Catal B: Environ 218, 9–19.
[53] Chen, W., Duan, G.-R., Liu, T.-Y., Chen, S.-M., Liu, X.-H., 2015. Fabrication of Bi_2MoO_6 nanoplates hybridized with g-C_3N_4 nanosheets as highly efficient visible light responsive heterojunction photocatalysts for Rhodamine B degradation. Mater Sci Semicond Process 35, 45–54.
[54] Fu, K., Pan, Y., Ding, C., Shi, J., Deng, H., 2021. Photocatalytic degradation of naproxen by Bi_2MoO_6/g-C_3N_4 heterojunction photocatalyst under visible light: mechanisms, degradation pathway, and DFT calculation. J Photochem Photobiol A: Chem 412.
[55] Wan, J., Huang, J., Yu, H., Liu, L., Shi, Y., Liu, C., 2021. Fabrication of self-assembled 0D–2D Bi2MoO6-g-C3N4 photocatalytic composite membrane based on PDA intermediate coating with visible light self-cleaning performance. J Colloid Interface Sci 601, 229–241.
[56] Wang, R., Ren, D., Xia, S., Zhang, Y., Zhao, J., 2009. Photocatalytic degradation of Bisphenol A (BPA) using immobilized TiO_2 and UV illumination in a horizontal circulating bed photocatalytic reactor (HCBPR). J Hazard Mater 169, 926–932.
[57] Fronczak, M., 2020. Adsorption performance of graphitic carbon nitride-based materials: current state of the art. J Environ Chem Eng 8.
[58] Wang, X., Wang, G., Chen, S., Fan, X., Quan, X., Yu, H., 2017. Integration of membrane filtration and photoelectrocatalysis on g-C_3N_4/CNTs/Al_2O_3 membrane with visible-light response for enhanced water treatment. J Membr Sci 541, 153–161.
[59] Wang, F., Chen, Z., Zhu, Z., Guo, J., 2022. Construction of visible light responsive ZnO/N-g-C_3N_4 composite membranes for antibiotics degradation. J Mater Res Technol 17, 1696–1706.
[60] Ramasundaram, S., Yoo, H.N., Song, K.G., Lee, J., Choi, K.J., Hong, S.W., 2013. Titanium dioxide nanofibers integrated stainless steel filter for photocatalytic degradation of pharmaceutical compounds. J Hazard Mater 258-259, 124–132.
[61] Horovitz, I., Avisar, D., Baker, M.A., Grilli, R., Lozzi, L., Di Camillo, D., Mamane, H., 2016. Carbamazepine degradation using a N-doped TiO_2 coated photocatalytic membrane reactor: influence of physical parameters. J Hazard Mater 310, 98–107.
[62] Kuo-Hua Wang*, H.-H.T., Hsieh, Yung-Hsu, 1998. The kinetics of photocatalytic degradation of trichloroethylene in gas phase over TiO_2 supported on glass bead. Appl Catal B: Environ 17, 313–320.
[63] Yamazaki-Nishida, K.J.N.S., Phillips, L.A., Cervera-March, S., Anderson, M.A., 1993. Photocatalytic degradation of trichloroethylene in the gas phase using titanium dioxide pellets. J Photochem Photobiol A: Chem 70, 95–99.
[64] Wang, Z., Liu, J., Dai, Y., Dong, W., Zhang, S., Chen, J., 2011. Dimethyl sulfide photocatalytic degradation in a light-emitting-diode continuous reactor: Kinetic and mechanistic study. Ind Eng Chem Res 50, 7977–7984.
[65] Herrmann, J.-M., 2010. Photocatalysis fundamentals revisited to avoid several misconceptions. Appl Catal B: Environ 99, 461–468.
[66] Yu, H., Zhang, K., Rossi, C., 2007. Theoretical study on photocatalytic oxidation of VOCs using nano-TiO_2 photocatalyst. J Photochem Photobiol A: Chem 188, 65–73.
[67] A.R.H.S.T. Liu, 1977. Determination of aqueous solubility and pKa values of estrogens. J Pharm Sci 66 (5), 624–627.
[68] Kumar, K.V., Porkodi, K., Rocha, F., 2008. Langmuir–Hinshelwood kinetics – a theoretical study. Catal Commun 9, 82–84.
[69] Wang, W.Y., Irawan, A., Ku, Y., 2008. Photocatalytic degradation of acid red 4 using a titanium dioxide membrane supported on a porous ceramic tube. Water Res 42, 4725–4732.
[70] Xu, X., Sun, Y., Fan, Z., Zhao, D., Xiong, S., Zhang, B., Zhou, S., Liu, G., 2018. Mechanisms for $^{\cdot}O_2$ and $^{\cdot}OH$ production on flowerlike $BiVO_4$ photocatalysis based on electron spin resonance. Front Chem 6, 64.
[71] Zhu, B., Xia, P., Ho, W., Yu, J., 2015. Isoelectric point and adsorption activity of porous g-C_3N_4. Appl Surf Sci 344, 188–195.
[72] Hurwitz, A.R., Liu, S.T., 1977. Determination of aqueous solubility and pKa values of estrogens. J Pharm Sci 66, 624–627.
[73] WHO, 1997. Guidelines for Drinking-water Quality, second ed. World Health Organization, Geneva.
[74] Brion, F., Le Page, Y., Piccini, B., Cardoso, O., Tong, S.K., Chung, B.C., Kah, O., 2012. Screening estrogenic activities of chemicals or mixtures in vivo using transgenic (cyp19a1b-GFP) zebrafish embryos. PLoS One 7, e36069.
[75] Yost, E.E., Meyer, M.T., Dietze, J.E., Meissner, B.M., Worley-Davis, L., Williams, C. M., Lee, B., Kullman, S.W., 2013. Comprehensive assessment of hormones, phytoestrogens, and estrogenic activity in an anaerobic swine waste lagoon. Environ Sci Technol 47, 13781–13790.
[76] Li, Y., Niu, J., Yin, L., Wang, W., Bao, Y., Chen, J., Duan, Y., 2011. Photocatalytic degradation kinetics and mechanism of pentachlorophenol based on superoxide radicals. J Environ Sci 23, 1911–1918.
[77] R.G.Pa.W. Yang, Density functional approach to the frontier-electron theory of chemical reactivity, Journal of the American Chemical Society, 16 (184) 4049–4050.
[78] Qing, Y., Li, Y., Cao, L., Yang, Y., Han, L., Dansawad, P., Gao, H., Li, W., 2023. Rationally designed C-PANI/BiOBr STEP-scheme heterojunction photocatalyst for boosting photodegradation of 17β-estradiol. Sep Purif Technol 314.
[79] Ali, H., Yasir, M., Ngwabebhoh, F.A., Sopik, T., Zandraa, O., Sevcik, J., Masar, M., Machovsky, M., Kuritka, I., 2023. Boosting photocatalytic degradation of estrone hormone by silica-supported g-C_3N_4/WO_3 using response surface methodology coupled with Box-Behnken design. J Photochem Photobiol A: Chem 441.
[80] Rokhina, E.V., Suri, R.P.S., 2012. Application of density functional theory (DFT) to study the properties and degradation of natural estrogen hormones with chemical oxidizers. Sci Total Environ 417-418, 280–290.
[81] Lyubimenko, R., Richards, B.S., Turshatov, A., Schafer, A.I., 2020. Separation and degradation detection of nanogram-per-litre concentrations of radiolabelled steroid hormones using combined liquid chromatography and flow scintillation analysis. Sci Rep 10, 7095.